Design and Control of a Novel Electromagnetic Actuated 3-DoFs Micropositioner

Xiao Xiao[1*] · Ruidong Xi[2*] · Yangmin Li[3] · Yirui Tang[2] · Bingxiao Ding[4] · Hongliang Ren[5] · Max. Q.-H. Meng[1]

Received: 4 Nov 2020 / Accepted: 10 Nov 2020

Abstract In this paper, a novel electromagnetic micropositioner is designed from an orthogonal 3-P(4S) parallel mechanism through the substitution method and modular design techniques. Preliminary prototype experiments show that the micropositioner possesses an excellent decoupling performance. Thus an independent control strategy is carried out for the motion control of the micropositioner. An RBF neural networks based adaptive backstepping terminal sliding mode controller is designed according to the nonlinearity characteristics of the actuator. Parameters of the system are identified with a genetic algorithm. Finally, the performances of the micropositioner and the developed control strategy are verified. Experimental results demonstrate that satisfactory performances can be achieved.

Keywords Micropositioner · Compliant mechanism · Electromagnetic actuator

Yangmin Li, Max. Q.-H. Meng
yangmin.li@polyu.edu.hk, mengqh@sustech.edu.cn

* X. Xiao and R. Xi contributed equally to this work.
[1] Department of Electrical and Electronic Engineering, Southern University of Science and Technology, Shenzhen, 518055, China.
[2] Department of Electromechanical Engineering, Faculty of Science and Technology, University of Macau, Macau SAR, China.
[3] Department of Industrial and Systems Engineering, The Hong Kong Polytechnic University, Hong Kong SAR, China.
[4] Department of Mechanical Engineering, Jishou University, 416000, China.
[5] Department of Biomedical Engineering, National University of Singapore, 117580, Singapore.

1 Introduction

A compliant mechanism is a special mechanical structure composed of flexible joints (Nguyen et al., 2019; Xiao et al., 2017). Unlike traditional rigid kinematic joint, a flexible joint is monolithic, so there is no clearance and no friction, which is beneficial for reducing the number of components and forming a miniaturized design (Mayyas and Mamidala, 2020). Most importantly, the elastic deformation of the flexible joint enables high repeatability and precision motion transmission (Kozuka et al., 2012). Based on these characteristics, compliant mechanisms contributed to various applications, such as micro/nanopositioning, manipulation, and manufacturing (Du et al., 2014; Kenton and Leang, 2012; Liu et al., 2014), multi-dimensional force-sensing (Li et al., 2018) and medical robot applications (Li et al., 2019a).

Compliant mechanism-based micropositioner (CMMP) is important in micro/nano-scaled positioning and manipulation applications (Clark et al., 2016; Wang et al., 2019), in particular, atomic force microscopy (AFM) and cell manipulation. As an essential tool in these fields, CMMP has attracted many researchers' attention since the last decade, and various micropositioning systems have been developed (Hajhashemi et al., 2011; Li et al., 2019b). Typically, there are two types of CMMP: (i) serial structural CMMP and (ii) parallel structural CMMP (Li et al., 2013). Parallel structure is preferred over serial structure due to advantages in terms of accuracy, rigidity, and load capability (Yang et al., 2019). Given difficulties in design and fabrication, most of the parallel CMMPs are limited to the planar degree of freedom (DoF) configuration. However, three translational DoFs are required in some applications. Although 6-DoFs CMMPs had been proposed (Dan and Rui, 2016; Lin et al., 2019), more DoFs im-

plies more actuators, which will increase the cost and the difficulty of control.

To solve this problem, Z. Zhu *et al* proposed a piezo-actuated triaxial compliant mechanism for nano cutting, which utilized an orthogonal chain configuration (Zhu et al., 2018). The stroke of each axis is around 12μm. J. Pinskier *et al* proposed a 4-DoFs serial-parallel hybrid haptic micromanipulator (Pinskier et al., 2018). By stacking a 1-DoF compliant mechanism on a 3-PRR CMMP, 4-DoFs, including three translational DoFs and one rotational DoF, were obtained. M. Ling *et al* proposed a PVDF sensing integrated piezo-actuated XYZ flexure manipulator, which also adopts the hybrid design to realize three translational DoFs by adding Z axis motion unit on a 2-DoFs CMMP (Ling et al., 2018). Another two classical CMMP designs can be found in the book chapter of T. J. Teo *et al.*(Joo et al., 2015). These designs have their advantages. However, considering compactness, isotropy, stroke, and cost, there is much improvement that can be done to fulfill specific applications (Ding et al., 2020).

Based on these considerations, we proposed an electromagnetic actuator (EMA) actuated CMMP, which has three translational DoFs. In our previous work (Xiao and Li, 2016), sliding mode control (SMC) of an EMA actuated compliant P joint was discussed. As an extension, this paper introduces the design and control of a more complicate EMA actuated system. Although the traditional SMC with the linear sliding surface has the merit of simple design procedure, this method only guarantees the asymptotical convergency. The convergence time cannot be obtained. In order to achieve the fast and finite-time convergence, a variant scheme named the terminal sliding mode control (TSMC) method is proposed (Man and Yu, 1996). In TSMC, a nonlinear sliding manifold is selected instead of the linear ones. Under such a mechanism, the rapid response and finite-time convergence could be assured. In the research work of (Chen et al., 2013), a kind of recursive terminal sliding manifold is introduced, which is efficient in the control of high order systems.

In this paper, a backstepping terminal sliding mode (BTSM) controller is designed according to the nonlinear characteristics of the EMA. With the utilize of the backstepping method, the robustness and the global convergence of the system can be guaranteed. To reduce the chattering phenomenon caused by the large switching items, an adaptive radial basis function (RBF) neural network is utilized to approximate the lumped disturbances. In this way, the system uncertainties, external disturbances, and the influence of the hysteresis are analyzed in this controller, by which the tracking accuracy could be further improved.

The main contributions of this paper can be summarized as: 1) A 3-DoFs parallel CMMP with compact structure is proposed, which has three decoupled translational DoFs; 2) A BTSM controller is developed for the three order nonlinear dynamics system of the proposed CMMP, which guarantees the global and fast convergence. An adaptive RBF neural network is also integrated into this controller to reduce the influence of the chattering phenomenon; 3) The feasibility of the EMA in micron accuracy level application is validated, which will provide a low-cost solution for micro positioning and manipulation.

In the rest of the paper, section II introduces the design of the CMMP. Section III presents the prototype of the proposed CMMP and the experimental setup. Preliminary experiments are carried out. In section IV, the design of the RBF neural networks based adaptive BTSM controller is presented, and parameter identification is illustrated in section V. Then, in section VI, tracking experiments are conducted to verify the performance of the CMMP and designed controller. At last, conclusion and future works are presented in section VII.

2 Design of the Micropositioner

Figure 1 (a) shows the schematic diagram of a parallel mechanism with traditional rigid linkage, which consists of three identical kinematic chains, a base, and a platform. The three chains are perpendicular to each other. Each chain has one active joint and four passive joints. The active joint and passive joint are prismatic (P) joint and spherical (S) joint, respectively. According to the configuration, we can call the parallel mechanism 3-P(4S) parallel mechanism. The most remarkable feature of the design is the embedded structure, which makes it compact and portable. Besides, it has three translational DoFs.

Based on the rigid 3-P(4S) parallel mechanism, a CMMP (Fig. 1 (c)) with the same configuration is proposed. The rigid linkages are replaced with compliant joints, and an EMA actuates each chain. The platform of the CMMP is set transparent so that the internal structure can be observed.

Figure 1 (b) shows the detailed structure of the kinematic chain of the CMMP. The armature and the EMA are fixed on the platform of the compliant P joint and the base of the CMMP with a distance of d_8, respectively. d_8 is the maximum allowable stroke of the compliant P joint. The dimensions of the compliant kinematic chain are listed in Table I.

The CMMP can be used for precision positioning application with the specimen or other targets placed

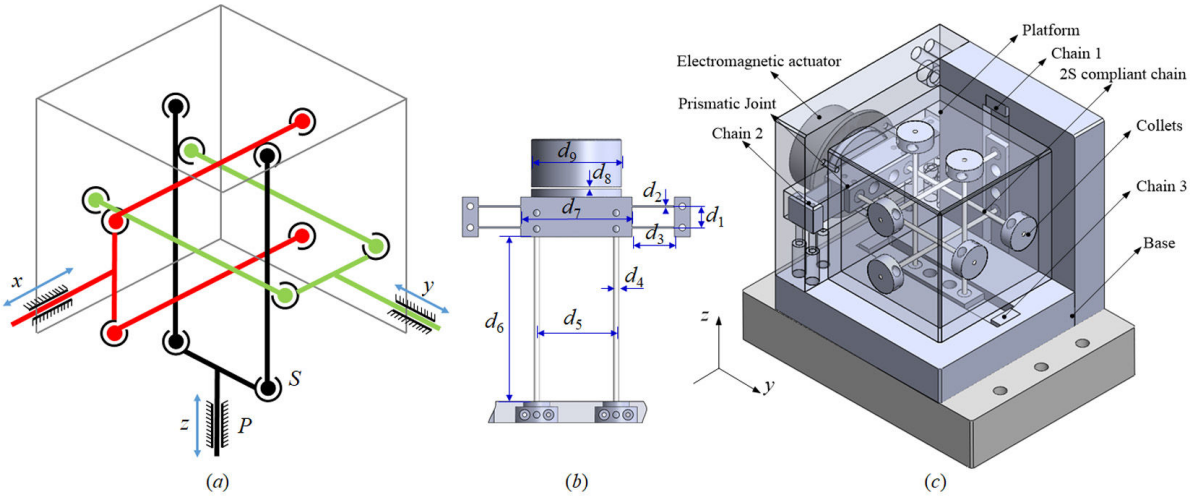

Fig. 1 Design of the CMMP. (a) Schematic diagram of 3-P(4S) parallel mechanism, (b) Kinematic chain of the CMMP, (c) 3D model of the proposed CMMP.

on the platform. It can also be used for micromanipulation application with a gripper attached on the platform.

Table 1 Parameters of the compliant P(4S) chain

Parameters	Variable	Value (mm)
Beam flexures center distance	d_1	8
Thickness of the beam flexure	d_2	0.6
Length of the beam flexure	d_3	16
Diameter of the rod flexure	d_4	2
Rod flexures center distance	d_5	30
Length of the rod flexure	d_6	62
Length of rigid part of P joint	d_7	42
Length of air gap	d_8	1
Diameter of the armature	d_9	32

3 Prototype Development and Preliminary Experiments

3.1 Experimental setup

A prototype of the proposed CMMP with optimized parameters is fabricated. The materials of the compliant P joint and the fully compliant 2S branch are AL 7075 and spring steel wire, respectively. Wire electrical-discharge machining (WEDM) is adopted to machine the compliant P joint, and other processes such as turnery and grinding are adopted to manufacture the rest parts. After this, precision assembling is conducted to construct the final prototype.

The experimental setup is shown in Fig. 2, which consists of four units: (1). Control & signal processing unit, (2). Driving unit, (3). Micropositioner, (4). Sensing unit. A dSPACE control system (from dSPACE GmbH Ltd.) together with an industrial PC (from Advantech Co., Ltd.) is adopted as the real-time control unit. To actuate the EMA (model: ZYE1-P34/18 from Yueqing Zhengyong Electrical, Inc.), a multi-channel power amplifier based on OPA548 is developed as the driving unit. The rated voltage and force of the EMA are 12v and 180N, respectively. To measure the motion of the CMMP, each axis is equipped with a high precision laser displacement sensor (model: LTC-025-02 from MTI, Inc.). In addition, a digital microscope (model: Supereyes T004 from D&F Co., Ltd) is adopted to observe the motion of the CMMP on the monitor. The CMMP, together with the laser displacement sensors, are fixed on an active vibration isolation table (from Newport, Inc.) to eliminate external vibrations. Besides, a modified Filand K220 joystick is developed as the master input device for manual control.

The signal flowchart of the micropositioning system is graphically explained in Fig. 3. Specifically, the control scheme is firstly realized in Matlab/Simulink, then complied and downloaded into a dSPACE control system through a real-time interface (RTI). Once the download is accomplished, a rapid control prototype (RCP) system is established. Control signals are generated by the dSPACE according to the control algorithm, then amplified by the 4-channel power amplifier. The platform of the CMMP will move when the EMAs are actuated. Movements of the platform can be detected by the laser displacement sensors and monitored by the digital microscope.

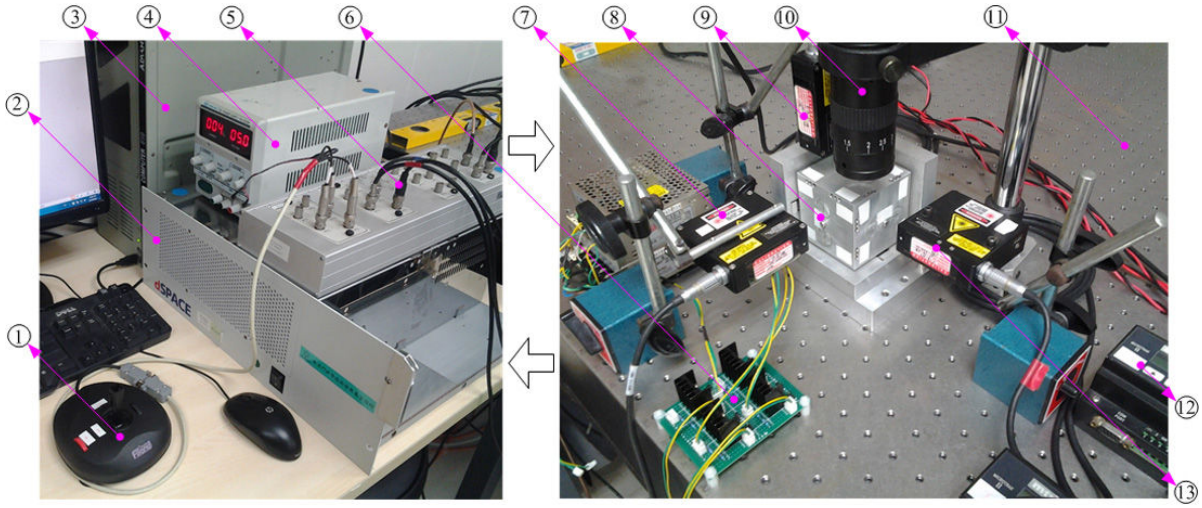

Fig. 2 Experimental setup 1. Joystick, 2. dSPACE, 3. Industrial PC, 4. DC power supply, 5. dSPACE interface, 6. EMA amplifier, 7. x-Laser displacement sensor, 8. Micropositioner, 9. z-Laser displacement sensor, 10. Digital microscope, 11. Active vibration isolation table, 12. Laser sensor controller, 13. y-Laser displacement sensor.

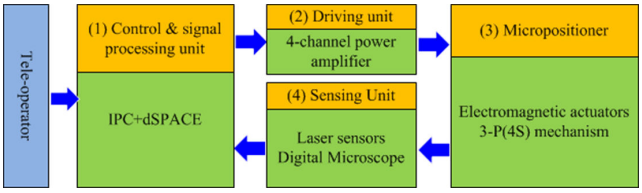

Fig. 3 System signal flow chart.

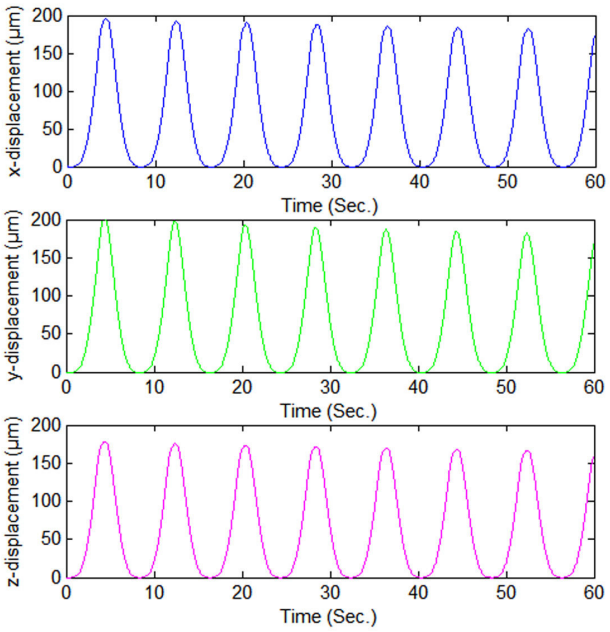

Fig. 4 Stroke tests of the three axes.

3.2 Preliminary Experiments

In this section, stroke, as well as the decoupling characteristic of the CMMP, are evaluate with preliminary experiments

Firstly, three open-loop experiments are carried out to test the stroke of the CMMP. In each test, only the EMA along the predominant direction is actuated. Periodical sine wave voltage signal (0.125Hz, 0-6v) is selected as the test signal. After amplification, the signal (0.125Hz, 0-12v) is transmitted to the EMA, the output displacement of the corresponding axis is recorded by the laser displacement sensor. Fig. 4 shows the results of three axial motions of the CMMP. The peak outputs are 195.6μm, 203.7μm, and 178.2μm, respectively. The distinction mainly results from different initial distance between the EMA and the armature caused by assembly errors.

Besides, the experimental results indicate that the peak outputs vary with time. Due to the electromagnetic coil is an inductive element, so the system is an RL low pass filter system. According to Lenz's law, the magnetic field of inductive current always resists the change of current flow through the coil. The faster the change, the higher the obstruction. So the decrease of the peak output is caused by the electromotive inductive in the coil. Thus, effective controller and closed-loop control should be adopted to improve the positioning performance of the CMMP.

Furthermore, a closed-loop test is conducted to verify the decoupling characteristics of the CMMP. During the experiment, each axis is controlled by a PID controller to track a sine wave trajectory (0.125Hz, 0-100μm). The three EMAs are actuated synchronously. The experimental results are illustrated in Fig. 5, where D stands for "desired". It can be observed that the errors are within $\pm 0.5\mu$m. Besides, the three axes are

controlled to track sine waves with different frequencies simultaneously (0.125Hz for the x-axis, 0.1Hz for the y-axis, 0.075Hz for z-axis), and the results are shown in Fig. 6. Both experimental results reveal an excellent decoupling performance. Thus, independent control strategy can be applied to control the motion of each axis.

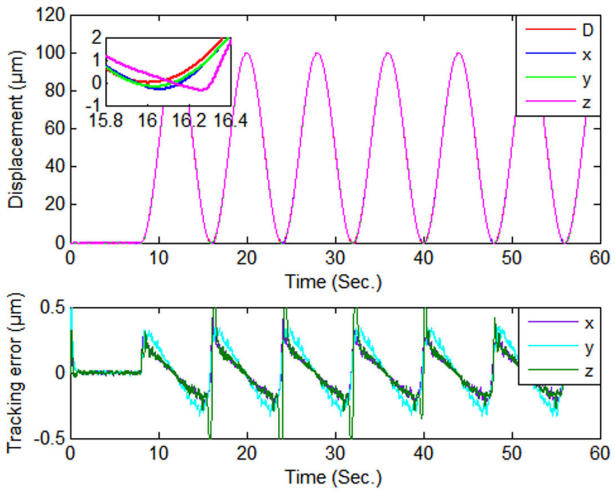

Fig. 5 Three axes trajectory tracking results with fixed frequency.

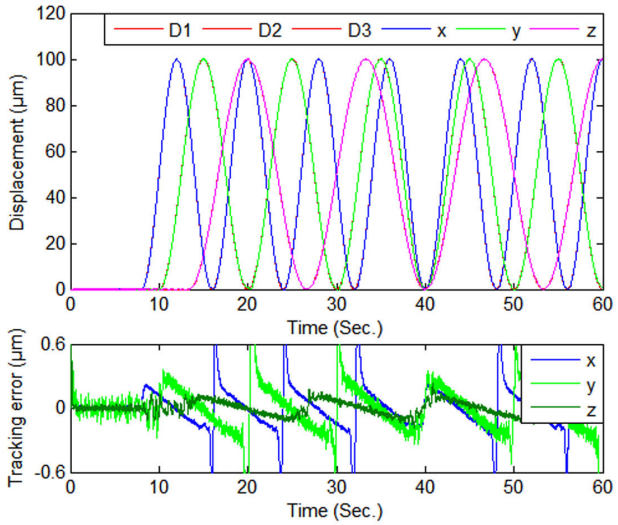

Fig. 6 Three axes trajectory tracking results with different frequencies.

4 Controller Design

Based on the experimental result, three single input single output (SISO) controllers are designed. As an illustration, an RBF neural networks based adaptive BTSM controller for the x-axis is implemented in this section.

The magnetic force generated by the EMA can be approximated by the following model.

$$F_m = c\left(\frac{i_c}{y+a}\right)^2 \tag{1}$$

where a and c are constants related to the actuator. i_c is the excitation current, y is the air gap, distance between the armature and the EMA.

Furthermore, the electrical model of the system can be established as

$$e = Ri_c + \frac{d}{dt}\left(Li_c\right) \tag{2}$$

where e is the voltage supplied to the EMA, R is the coil resistance, L is the coil inductance which can be expressed as

$$L{=}L_1 + \frac{aL_0}{y+a} \tag{3}$$

where L_1 is the inductance when the air gap is infinite, and L_0 is the incremental inductance when air gap is zero.

The equation of motion for the single axis EMA actuated system can be written as

$$m\frac{d^2y}{dt^2} = k\left(\delta_0 - y\right) - F_m \tag{4}$$

where k is the stiffness of the system, δ_0 is the initial air gap.

Equations (2)-(4) are the dynamic model for the single axis EMA actuated system. Let the state variables be $x_1 = y$, $x_2 = \dot{y}$, $x_3 = i_c$, and the control input be $u = e$. Then the state-space model can be written as

$$\begin{aligned}
\dot{x}_1 &= x_2, \\
\dot{x}_2 &= \frac{k}{m}\left(\delta_0 - x_1\right) - \frac{c}{m}\left(\frac{x_3}{x_1+a}\right)^2, \\
\dot{x}_3 &= \frac{1}{L}\left(-Rx_3 + \frac{L_0 a x_2 x_3}{\left(x_1+a\right)^2} + u\right).
\end{aligned} \tag{5}$$

In order to transform the state-space model into canonical form, the following nonlinear transformation are made.

$$\begin{aligned}
z_1 &= x_1, \\
z_2 &= x_2, \\
z_3 &= \frac{k}{m}\left(\delta_0 - x_1\right) - \frac{c}{m}\left(\frac{x_3}{x_1+a}\right)^2.
\end{aligned} \tag{6}$$

Then we can have

$$\begin{aligned}\dot{z}_1 &= z_2,\\ \dot{z}_2 &= z_3,\\ \dot{z}_3 &= f(x) + g(x)\,u\end{aligned} \tag{7}$$

where

$$f(x) = -\frac{kx_2}{m} + \frac{2cx_3^2}{m(x_1+a)^2}\left(\frac{L(x_1+a)-aL_0}{L(x_1+a)^2}x_2 + \frac{R}{L}\right),$$

$$g(x) = -\frac{2cx_3}{Lm(x_1+a)^2}.$$

When z_1, z_2, z_3 are driven to zero, x_1, x_2 and x_3 will converge to x_{1d}, zero and $(x_{1d}+a)\sqrt{k(\delta_0 - x_{1d})/c}$, respectively, where x_{1d} is the desired position of the platform.

Considering the system uncertainties, external disturbances and hysteresis, the system can be rewritten as:

$$\begin{cases}\dot{z}_1 = z_2\\ \dot{z}_2 = z_3\\ \dot{z}_3 = f_0(x) + g_0(x)u + (\Delta f + \Delta g u) + d + \rho\end{cases} \tag{8}$$

where $f_0(x)$, $g_0(x)$ are nominal part of $f(x)$, $g(x)$, $\Delta f = f(x) - f_0(x)$ and $\Delta g = g(x) - g_0(x)$ denote the uncertainties of the system; d is the external disturbances and ρ presents the hysteresis in the driving system. Taking all the uncertainties, disturbances and hysteresis as lumped disturbances, we have

$$\begin{cases}\dot{z}_1 = z_2\\ \dot{z}_2 = z_3\\ \dot{z}_3 = f_0(x) + g_0(x)u + D\end{cases} \tag{9}$$

where D denotes the lumped system disturbances.

4.1 BTSM controller

In order to achieve fast transient response and finite-time convergence, a recursive terminal sliding manifold is selected as (**?**):

$$\begin{cases}s_0 = e\\ s_1 = \dot{s}_0 + \alpha_0 s_0 + \beta_0 s_0^{q_0/p_0}\\ s_2 = \dot{s}_1 + \alpha_1 s_1 + \beta_1 s_1^{q_1/p_1}\end{cases} \tag{10}$$

where $e = z_d - z_1$ denotes the tracking error, α_0, β_0, α_1, β_1, p_0, q_0, p_1, q_1 are designed parameters with $p_i > q_i, i = 1, 2$ and both p_1, q_1 are positive odd integers.

Calculating the first and second order derivative of s_1 and time derivative of s_2, one can get:

$$\dot{s}_1 = \ddot{s}_0 + \alpha_0\dot{s}_0 + \beta_0\frac{q_0}{p_0}s_0^{(\frac{q_0}{p_0}-1)}\dot{s}_0 \tag{11}$$

$$\ddot{s}_1 = \dddot{s}_0 + \alpha_0\ddot{s}_0 + \beta_0\frac{q_0}{p_0}s_0^{(\frac{q_0}{p_0}-1)}\ddot{s}_0 + \beta_0\frac{q_0(q_0-p_0)}{p_0^2}s_0^{(\frac{q_0}{p_0}-2)}\dot{s}_0^2 \tag{12}$$

$$\dot{s}_2 = \ddot{s}_1 + \alpha_1\dot{s}_1 + \beta_1\frac{q_1}{p_1}s_1^{(\frac{q_1}{p_1}-1)}\dot{s}_1 \tag{13}$$

From the system model, we know that

$$\dddot{s}_0 = \dddot{z}_d - (f_0(x) + g_0(x)u + D) \tag{14}$$

Taking (11), (12), (14) into (13), one can obtain

$$\dot{s}_2 = \dddot{z}_d - (f_0(x) + g_0(x)u + D) + \Psi(s_0, \dot{s}_0, \ddot{s}_0, s_1, \dot{s}_1) \tag{15}$$

where

$$\Psi(s_0, \dot{s}_0, \ddot{s}_0, s_1, \dot{s}_1) = \alpha_0\ddot{s}_0 + \beta_0\frac{q_0}{p_0}s_0^{(\frac{q_0}{p_0}-1)}\ddot{s}_0 + \beta_0\frac{q_0(q_0-p_0)}{p_0^2}s_0^{(\frac{q_0}{p_0}-2)}\dot{s}_0^2 + \alpha_1\dot{s}_1 + \beta_1\frac{q_1}{p_1}s_1^{(\frac{q_1}{p_1}-1)}\dot{s}_1$$

To proceed the design of the controller, the classical Lemma 1 is introduced (Chen et al., 2013).

Lemma 1. For a positive definite function $L(t)$, which satisfies the following inequality:

$$\dot{L}(t) + \alpha L(t) + \lambda L^{\gamma}(t) \le 0, \forall t > t_0 \tag{16}$$

Then $L(T)$ converges to the equilibrium point in finite time t_s

$$t_s \le t_0 + \frac{1}{\alpha(1+\gamma)}ln\frac{\alpha L^{1-\gamma}(t_0) + \lambda}{\lambda} \tag{17}$$

where $\alpha > 0$, $\lambda > 0$, $0 < \gamma < 1$.

In order to obtain an efficient control input, the backstepping design procedure will be employed.

Step 1: Define a Lyapunov candidate $V_1 = \frac{1}{2}s_1^2$, and differentiating V_1 respect to time, one can get

$$\begin{aligned}\dot{V}_1 &= s_1(s_2 - \alpha_1 s_1 - \beta_1 s_1^{q_1/p_1})\\ &= -\alpha_1 s_1^2 - \beta_1 s_1^{(\frac{p_1+q_1}{p_1})} + s_1 s_2\end{aligned} \tag{18}$$

From (18) we can see that while $s_2 = 0$,

$$\dot{V}_1 = -\alpha_1 s_1^2 - \beta_1 s_1^{(\frac{p_1+q_1}{p_1})} \tag{19}$$

which implies s_1 will be finite convergent according to Lemma 1.

Step 2: Define a Lyapunov candidate $V_2 = V_1 + \frac{1}{2}s_2^2$, and differentiating V_2 respect to time, we have

$$\dot{V}_2 = -\alpha_1 s_1^2 - \beta_1 s_1^{(\frac{p_1+q_1}{p_1})} + s_1 s_2 + s_2[\dddot{z}_d - (f_0(x) + g_0(x)u + D) + \Psi(s_0, \dot{s}_0, \ddot{s}_0, s_1, \dot{s}_1)]$$

(20)

Then the BTSM controller is designed as:

$$u_b = \frac{1}{g_0(x)}(\dddot{z}_d - f_0(x) + \Psi(s_0, \dot{s}_0, \ddot{s}_0, s_1, \dot{s}_1) + s_1 + \xi_1 s_2 + \beta_2 s_2^{(\frac{p_1+q_1}{p_1})} + K sign(s_2)) \tag{21}$$

where β_2 is a designed positive parameter.

Taking (21) into (20), we have

$$\dot{V}_2 = -\alpha_1 s_1^2 - \beta_1 s_1^{(\frac{p_1+q_1}{p_1})} - \xi_1 s_2^2 - \beta_2 s_2^{(\frac{p_1+q_1}{p_1})} - D s_2 - K|s_2| \tag{22}$$

From (22), we know that if $K \geq |\bar{D}|$, $\bar{D}$ is the upper bound of D, the stability of the system can be guaranteed. Whereas, a too-large value of K will induce a severe chattering phenomenon, thus an RBF neural networks based complement of the external disturbances $\hat{D}$ will be introduced in the controller.

4.2 RBF neural networks based adaptive BTSM controller

Using RBF neural networks to approximate D, the expression of D yields

$$D = Wh(x) + \varepsilon \tag{23}$$

where W is the optimal weight vector, $h(x)$ is the basis function vector and ε is the approximation error. The output of the RBF neural networks is

$$\hat{D} = \hat{W}h(x) \tag{24}$$

Define $\tilde{W} = W - \hat{W}$, $||W||_F \leq W_{\max}$, then

$$D - \hat{D} = \tilde{W}h(x) + \varepsilon \tag{25}$$

The control input of RBF neural networks based adaptive BTSM controller is designed as:

$$u = \frac{1}{g_0(x)}(\dddot{z}_d - f_0(x) + \Psi(s_0, \dot{s}_0, \ddot{s}_0, s_1, \dot{s}_1) + s_1 + \beta_2 s_2^{(\frac{q_1+p_1}{p_1})} - \hat{D} + \xi_1 s_2 + k_w sign(s_2)) \tag{26}$$

with

$$\dot{\hat{W}} = -\Lambda^{-1} h(x) s_2 \tag{27}$$

Theorem 1. For the dynamics model (9) subject to system uncertainties, external disturbances, and hysteresis, under the RBF neural networks based adaptive BTSM control input (25) with the adaptive law (26), the finite time convergence of the closed-loop system is guaranteed.

Proof: Considering the Lyapunov function

$$V = V_2 + \tfrac{1}{2} tr(\tilde{W}^T \Lambda \tilde{W}) \tag{28}$$

where Λ is a designed positive diagonal matrix.

Invoking (22), (26), (27) and differentiating V with respect to time, we have

$$\begin{aligned}
\dot{V} =& -\alpha_1 s_1^2 - \beta_1 s_1^{(\frac{p_1+q_1}{p_1})} - \xi_1 s_2^2 - \beta_2 s_2^{(\frac{p_1+q_1}{p_1})} \\
& - (D - \hat{D}) s_2 - k_w |s_2| + tr(\tilde{W}^T \Lambda \dot{\tilde{W}}) \\
=& -\alpha_1 s_1^2 - \beta_1 s_1^{(\frac{p_1+q_1}{p_1})} - \xi_1 s_2^2 - \beta_2 s_2^{(\frac{p_1+q_1}{p_1})} \\
& - \tilde{W}h(x) s_2 - \varepsilon s_2 - k_w |s_2| + tr(\tilde{W}^T \Lambda \dot{\tilde{W}}) \\
=& -\alpha_1 s_1^2 - \beta_1 s_1^{(\frac{p_1+q_1}{p_1})} - \xi_1 s_2^2 - \beta_2 s_2^{(\frac{p_1+q_1}{p_1})} \\
& - tr\tilde{W}^T (h(x) s_2 + \Lambda \dot{\hat{W}}) - \varepsilon s_2 - k_w |s_2| \\
=& -\alpha_1 s_1^2 - \beta_1 s_1^{(\frac{p_1+q_1}{p_1})} - \xi_1 s_2^2 - \beta_2 s_2^{(\frac{p_1+q_1}{p_1})} \\
& - \varepsilon s_2 - k_w |s_2|
\end{aligned} \tag{29}$$

Can be seen that if $k_w \geq |\bar{\varepsilon}|$, where $\bar{\varepsilon}$ is the upper bound of ε, $\dot{V} \leq 0$. $\dot{V}$ is negative semidefinite, which means that s_1 and s_2 will converge to zero in finite time. Therefore, the proposed adaptive BTSM system is stable with the existence of system uncertainties, external disturbances, and hysteresis.

5 System parameters identification

As indicated in Eq. (5), the system model contains several unknown parameters. This is a commonly encountered issue in control engineering, and the necessity to address this problem has been widely recognized. Although several methods have been developed, it is difficult to identify the nonlinear system by using conventional approaches. System identification based on evolutionary algorithms is regarded as a promising solution due to their global and parallel searching ability. So genetic algorithm (GA) is introduced for parameter identification in this paper.

Identification is the process of developing an accurate mathematical model for a system through input and output data. Thus, experiments are carried out in advance to collect the required data. The input is a multiamplitude sine-wave voltage signal, while the output is the displacement of the platform and current flowing through the coil. A current sensor (HBC01AS5) is adopted to record the current of the coil during the data acquisition experiment.

The fitness function is defined as below

$$F\left(L_1, L_0, a, R, c, k, m\right) = \sum_{n=1}^{N} \left(y_n - \hat{y}_n\right)^2 \tag{30}$$

where N is the number of the samples. y_n and $\hat{y}_n$ are measured and simulated output at the nth sampling time, respectively.

An initial population (50 individuals) is created by generating real-coded uniformly distributed random numbers within the feasible region. After which, each individual is assigned to the parameter set, and the Simulink model is repeatedly executed until the fitness value of every individual is evaluated. According to the rules of survival of the fittest, the population is constantly updated through GA operation. The process will continue until the optimal solution is obtained.

The parameters of the three axes are identified separately by the same way, and the identified parameters are listed in Table II.

Table 2 Identified parameters

Notation	x axis	y axis	z axis	Unit
L_1	13.47	13.21	12.95	H
L_0	0.65	0.67	0.68	H
a	1.11×10^{-5}	1.11×10^{-5}	1.11×10^{-5}	m
R	31.83	31.60	31.42	Ω
c	2.36×10^{-4}	2.37×10^{-4}	2.25×10^{-4}	$\mathrm{Nm^2A^{-}}$
k	2.22×10^{5}	2.21×10^{5}	2.26×10^{5}	$\mathrm{Nm^{-1}}$
m	0.451	0.450	0.443	Kg

6 Experimentation and discussion

In this section, to verify the performances of the designed controller and the CMMP, positioning and tracking experiments are carried out. Four complex spatial trajectories are designed. The four trajectories cover the whole workspace. For each trajectory, the speed, acceleration, and motion direction vary with time. The complexity can well test the performances of the controller and CMMP.

Figure 7 shows the tracking results of the cylindrical spiral trajectory. It starts with a linear contour from home position (0,0,0) to start position (40,0,0) with a speed of 8μm/s. Then it begins to track the cylindrical spiral, the diameter and pitch of which is 80μm and 20μm, respectively. The process has lasted 30 seconds with a fixed angular velocity of 0.25πrad/s. Finally, it returns to the origin along a slope line in yoz-plane. The tracking errors of the three axial motions are demonstrated in Fig. 7, which fluctuates within $\pm$0.03μm.

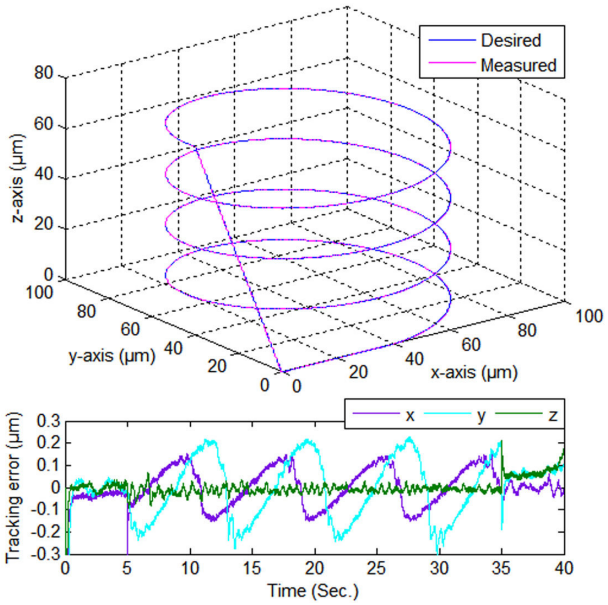

Fig. 7 Cylindrical spiral tracking results.

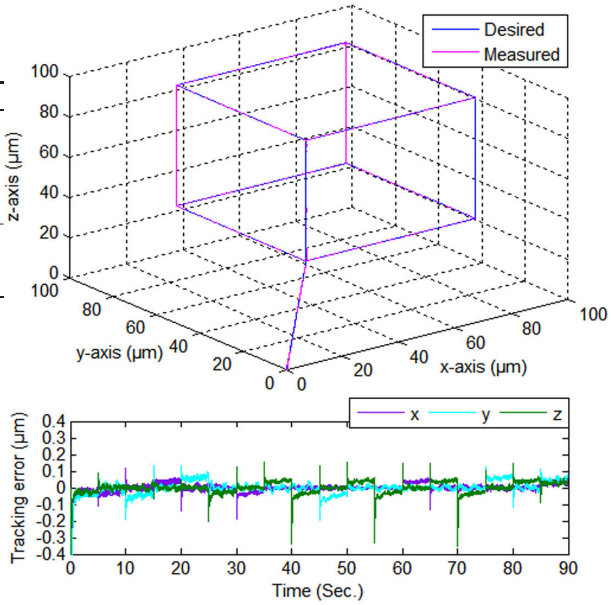

Fig. 8 Hexahedral edges tracking results.

Figure 8 shows the hexahedral edges tracking results. The home position and the start position are set as (0,0,0) and (30,30,30), respectively. The contour is accomplished through three stages. Specifically, the first stage (0-5s) from home position to start position and the third stage (85s-90s) from the end position to home position is connected by the cubical stage (5s-85s). To implement the cubic shape at one time, each vertical edge is performed twice. So the second stage is divided into 16 steps (12 edges and 4 extra). The length of the edge is 60μm, and the feed-rate is 12μm/s. As can be observed, the CMMP tracks the desired trajectory with

a deviation of $\pm 0.4\mu$m, and the maximum error occurs at the vertexes, where motion direction and speed experience suddenly changes.

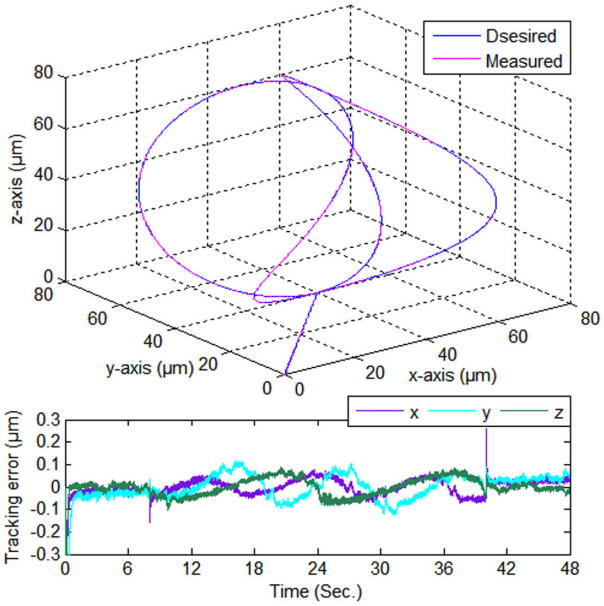

Fig. 9 Spatial quadrifolium tracking results.

Tracking results of the spatial quadrifolium is illustrated in Fig. 9. The parametric equations of the curve is defined as

$$\begin{cases} x = 40\sin(\pi - \pi t/8)\cos(0.125\pi t/2) + 40 \\ y = 40\sin(\pi - \pi t/8)\sin(0.125\pi t/2) + 40 \\ z = 40\cos(\pi - \pi t/8) + 40 \end{cases} \tag{31}$$

where we can find that the start position is (40,40,0), and the cycle is 32s.

As demonstrated in Fig. 9, except for two particular times (8s and 40s), the tracking errors of the three axes maintain within $\pm 0.2\mu$m. The sudden fluctuations of the tracking errors of the x-axis lie in discontinuous switching of the velocity and acceleration.

To further explore the 3D positioning performance of the CMMP, a spherical helix test is performed. The radius of the spherical is 40μm, and the start position is (40,40,0). 8 cycles of screw motion are needed to reach the end position. As shown in Fig. 10, the CMMP tracks the desired trajectory within $\pm 0.3\mu$m errors. More details of the experiments can be found in the attached video.

The results of the experiments indicate very good tracking performances. The positioning accuracy of the CMMP is better than 0.1μm for linear trajectory, and 0.5μm for other trajectories. The errors may come from machining errors, assembly errors, and Abbe error. Nevertheless, the performances will be further improved

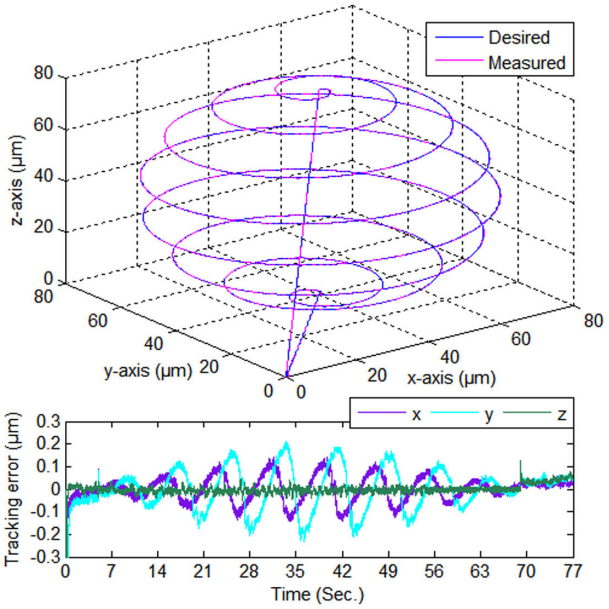

Fig. 10 Spherical helix tracking results.

if better machining, control, and measurement methods are introduced. In addition, sudden changes in the velocity, acceleration, and direction should be avoided during the trajectory planning. On considering the obtained experimental results, we can conclude that the proposed CMMP has the potential to be used in high precision micro/nanomanipulation applications.

7 Conclusion

An electromagnetic actuated 3-DoFs micropositioner is introduced in this paper, which is designed based on a rigid orthogonal 3-P(4S) parallel mechanism. Both analysis and experiments indicate that the proposed micropositioner possesses a good decoupling performance, based on which an independent control strategy is designed. Due to nonlinearities of the electromagnetic actuators, three RBF neural networks based adaptive BTSM controllers are developed to separately control the motions of the three axes after the unknown parameters of the system model are identified. Performances of the micropositioner are verified through complex spatial curve tracking experiments. The experimental results reveal that sub half micron positioning accuracy can be obtained, which indicate very satisfactory performances of the micropositioner and the developed controllers.

Acknowledgements This work was supported in part by National Natural Science Foundation of China (51575544).

References

Chen M, Wu QX, Cui RX (2013) Terminal sliding mode tracking control for a class of SISO uncertain nonlinear systems. ISA Trans 52(2):198–206

Clark L, Shirinzadeh B, Tian Y, Yao B (2016) Development of a passive compliant mechanism for measurement of micro/nanoscale planar 3-DOF motions. IEEE/ASME Transactions on Mechatronics 21(3):1222–1232

Dan W, Rui F (2016) Design and nonlinear analysis of a 6-DOF compliant parallel manipulator with spatial beam flexure hinges. Precision Engineering 45:365–373

Ding BX, Yang ZX, Li YM (2020) Design of flexure-based modular architecture micro-positioning stage. Microsystem Technologies 26(4):2893–2901

Du Z, Shi R, Dong W (2014) A piezo-actuated high-precision flexible parallel pointing mechanism: conceptual design, development, and experiments. IEEE Transactions on Robotics 30(1):131–137

Hajhashemi MS, Barazandeh F, Nazari Nejad S, Nadafi DB R (2011) Design and microfabrication of a constant-force microgripper. Proceedings of the Institution of Mechanical Engineers, Part C: Journal of Mechanical Engineering Science 225(11):2739–2748

Joo T, Yang GL, Chen IM (2015) Compliant manipulators, Springer-Verlag London Ltd, pp 2229–2300. Handbook of Manufacturing Engineering and Technology

Kenton BJ, Leang KK (2012) Design and control of a three-axis serial-kinematic high-bandwidth nanopositioner. IEEE/ASME Transactions on Mechatronics 17(2):356–369

Kozuka H, Arata J, Okuda K, Onaga A, Ohno M, Sano A, Fujimoto H (2012) A bio-inspired compliant parallel mechanism for high-precision robots. In: IEEE International Conference on Robotics and Automation (ICRA), Saint Paul, MN, USA, pp 3122–3127

Li CS, Gu X, Xiao X, Lim CM, Ren H (2019a) Flexible robot with variable stiffness in transoral surgery. IEEE/ASME Transactions on Mechatronics Doi: 10.1109/TMECH.2019.2945525

Li CX, Gu GY, Yang MJ, Zhu LM (2013) Design, analysis and testing of a parallel-kinematic high-bandwidth XY nanopositioning stage. Rev Sci Instrum 84(12):125111.1–13

Li JP, Huang H, Morita T (2019b) Stepping piezoelectric actuators with large working stroke for nanopositioning systems: A review. Sensors and Actuators A: Physical 292:39–51

Li T, Shi C, Ren H (2018) A high-sensitivity tactile sensor array based on fiber bragg grating sensing for tissue palpation in minimally invasive surgery. IEEE/ASME Transactions on Mechatronics 23(5):2306–2315

Lin C, Zheng S, Li P, Shen Z, Wang S (2019) Positioning error analysis and control of a piezo-driven 6-DOF micro-positioner. Micromachines (Basel) 10(8):542.1–20

Ling MX, Cao JY, Li QS, Zhuang J (2018) Design, pseudostatic model, and PVDF-based motion sensing of a piezo-actuated XYZ flexure manipulator. IEEE/ASME Transactions on Mechatronics 23(6):2837–2848

Liu J, Gong Z, Tang K, Lu Z, Ru C, Luo J, Xie S, Sun Y (2014) Locating end-effector tips in robotic micromanipulation. IEEE Transactions on Robotics 30(1):125–130

Man Z, Yu XH (1996) Terminal sliding mode control of MIMO linear systems. In: Proceedings of 35th IEEE Conference on Decision and Control, Kobe, Japan, pp 4619–4624

Mayyas M, Mamidala I (2020) Prosthetic finger based on fully compliant mechanism for multi-scale grasping. Microsystem Technologies DOI 10.1007/s00542-020-05045-8

Nguyen DN, Ho NL, Dao TP, Le Chau N (2019) Multi-objective optimization design for a sand crab-inspired compliant microgripper. Microsystem Technologies 25(10):3991–4009, DOI 10.1007/s00542-019-04331-4

Pinskier J, Shirinzadeh B, Clark L, Qin YD (2018) Development of a 4-DOF haptic micromanipulator utilizing a hybrid parallel-serial flexure mechanism. Mechatronics 50:55–68

Wang F, Shi B, Tian Y, Huo Z, Zhao X, Zhang D (2019) Design of a novel dual-axis micromanipulator with an asymmetric compliant structure. IEEE/ASME Transactions on Mechatronics 24(2):656–665

Xiao X, Li YM (2016) Development of an electromagnetic actuated microdisplacement module. IEEE/ASME Transactions on Mechatronics 21(3):1252–1261

Xiao X, Li YM, Xiao SL (2017) Development of a novel large stroke 2-dof micromanipulator for micro/nano manipulation. Microsystem Technologies 23(7):2993–3003

Yang M, Zhang C, Yang GL, Dong W (2019) Optimal design and tracking control of a superelastic flexure hinge based 3-PRR compliant parallel manipulator. IEEE Access 7:174236–174247

Zhu Z, To S, Zhu WL, Li YM, Huang P (2018) Optimum design of a piezo-actuated triaxial compliant mechanism for nanocutting. IEEE Transactions on Industrial Electronics 65(8):6362–6371